THE JOURNAL OF PHYSICAL CHEMISTRY B
A JOURNAL OF THE AMERICAN CHEMICAL SOCIETY

pubs.acs.org/JPCB

Article

Solvent Structure and Dynamics near the Surfaces of β-Hematin Crystals

Published as part of The Journal of Physical Chemistry virtual special issue "Dor Ben-Amotz Festschrift".

Laksmanji Verma, Peter G. Vekilov,* and Jeremy C. Palmer*

Cite This: *J. Phys. Chem. B* 2021, 125, 11264–11274

Read Online

ABSTRACT: Hematin crystallization, which is an essential component of the physiology of malaria parasites and the most successful target for antimalarial drugs, proceeds in mixed organic–aqueous solvents both *in vivo* and *in vitro*. Here we employ molecular dynamics simulations to examine the structuring and dynamics of a water–normal octanol mixture (a solvent that mimics the environment hosting hematin crystallization *in vivo*) in the vicinity of the typical faces in the habit of a hematin crystal. The simulations reveal that the properties of the solvent in the layer adjacent to the crystal are strongly impacted by the distinct chemical and topological features presented by each crystal face. The solvent organizes into at least three distinct layers. We also show that structuring of the solvent near the different faces of β-hematin strongly impacts the interfacial dynamics. The relaxation time of *n*-octanol molecules is longest in the contact layers and correlates with the degree of structural ordering at the respective face. We show that the macroscopically homogeneous water–octanol solution holds clusters of water and *n*-octanol connected by hydrogen bonds that entrap the majority of the water but are mostly smaller than 30 water molecules. Near the crystal surface the clusters anchor on hematin carboxyl groups. These results provide a direct example that solvent structuring is not restricted to aqueous and other hydrogen-bonded solutions. Our findings illuminate two fundamental features of the mechanisms of hematin crystallization: the elongated shapes of natural and synthetic hematin crystals and the stabilization of charged groups of hematin and antimalarials by encasing in water clusters. In addition, these findings suggest that hematin crystallization may be controlled by additives that disrupt or reinforce solvent structuring.

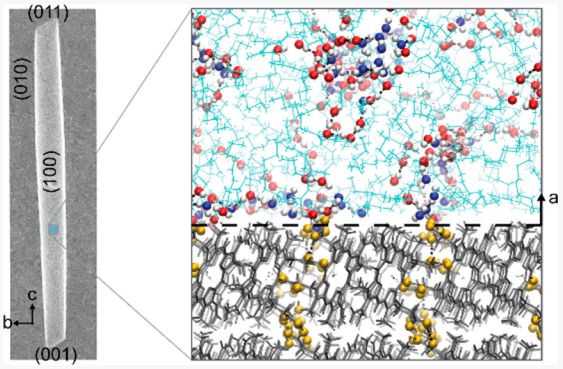

INTRODUCTION

During the intraerythrocytic stage of its life cycle, the malaria parasite feeds on the hemoglobin in the cytosol of the host's red blood cells.[1−4] Each hemoglobin molecule carries four iron-containing prosthetic groups, hemes, which are released as hemoglobin is digested and promptly converted to hematin, where iron is in its stable Fe^{3+} form (Figure 1a). Hematin catalyzes oxidation of essential parasite proteins and lipids and thus is highly toxic to the parasite.[5−7] To survive, the parasite sequesters hematin into innocuous crystals that present as intensely dark brown spots in the infected red blood cells and are known as malaria pigment or hemozoin (Figure 1b).[1,8−10] Hemozoin formation by hematin crystallization constitutes the process of the parasite physiology most vulnerable to antimalarial drugs and is sometimes referred to as the parasite's "Achilles heel". The drugs suppress hematin crystallization and boost the concentration of hematin above the toxicity level.[11] The parasite digestive vacuole, in which hemoglobin is catabolized, is largely filled with an aqueous solution of the proteolysis enzymes.[10,1220] Hemozoin, however, likely assembles in nanodroplets of neutral lipids that comprise a second liquid phase within the digestive vacuole;[21−26] an alternative proposal that hemozoin grows in the aqueous subphase without assistance from lipids[15,17] appears less feasible.[23] These lipid structures may hold up to 15 wt % water invading from the surrounding aqueous solution,[23] a crucial component for the hydrogen and coordination bonds that uphold the hemozoin crystal structure.[26,27]

The synthetic analogue of hemozoin is known as β-hematin (Figure 1c). To explore the crystallization of β-hematin, the mixture of neutral lipids found in the parasite's digestive vacuole is typically replaced with normal 1-octanol, which saturates with water at about 5 wt %.[23,24,26,28,29] Despite many years of research on hemozoin and β-hematin crystalliza-

Received: July 24, 2021
Revised: September 9, 2021
Published: October 5, 2021

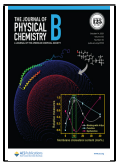

https://doi.org/10.1021/acs.jpcb.1c06589
J. Phys. Chem. B 2021, 125, 11264–11274

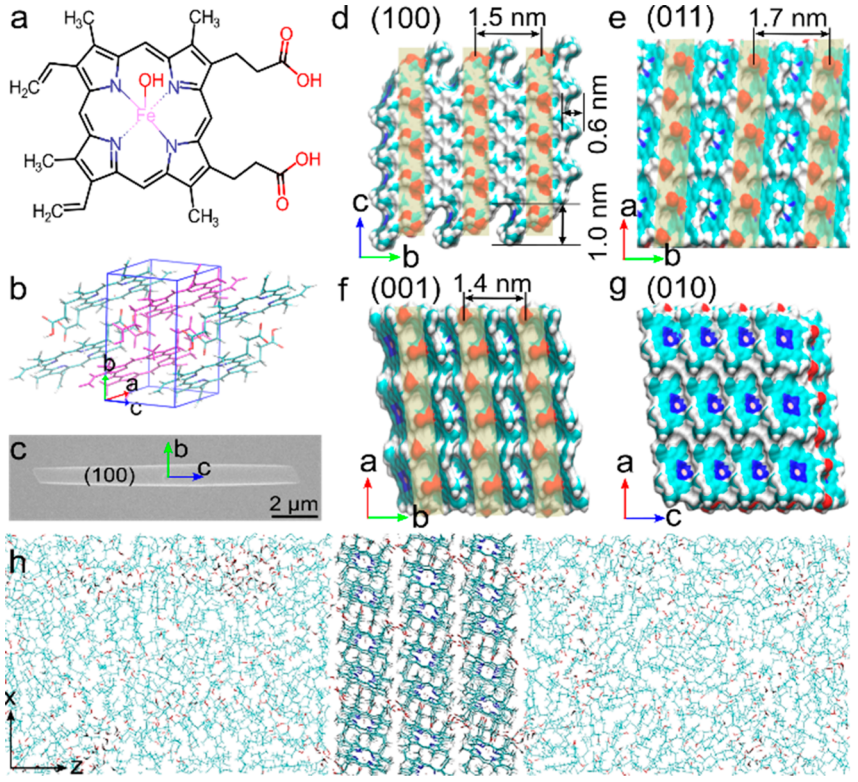

Figure 1. Structure of hematin and β-hematin crystals. (a) Molecular structure of hematin, the building block of β-hematin. Hematin has two propionic side chains with carboxyl groups (red) and an iron core (pink) coordinated by four nitrogen atoms (blue). (b) A unit cell of β-hematin highlighting the crystallographic hematin dimer (mauve). (c) SEM micrograph of a hematin crystal. The crystallographic directions and basal (100) face are labeled. (d–g) Top view of the structures of the (100), (011), and (001), and (010) faces of β-hematin. (d–f) The (100), (011), and (001) faces are patterned with alternating stripes of polar carboxyl groups (highlighted in beige) and nonpolar methyl and methylene groups. Whereas the (100) and (011) faces are relatively flat, the (001) face has ~1.0 nm deep grooves, evident when viewing the crystal along the [100] direction in (d). The polar groups reside on the inside ledges of the grooves. The center-to-center spacing between polar stripes is 1.5, 1.7, and 1.4 nm, and the overall carboxyl surface density is 0.85, 1.00, and 1.16 groups per nm^2 for the (100), (011), and (001) faces, respectively. (g) The (010) surface exposes only nonpolar groups and exhibits shallow grooves ~0.6 nm deep, evident when viewing the crystal along the [100] direction in (d). (h) Example of the slab geometry used for the molecular dynamics simulations. The β-hematin crystal is cleaved and reoriented to expose two identical faces to the solvent, with the surface normal aligned along the major axis (z-axis) of the simulation cell. The periodicity of the β-hematin crystal is retained along the minor (x- and y-) axes of the simulation cell. In (d), (e), (f), (g), and (h) oxygen is shown in red, nitrogen in blue, carbon in cyan, iron in purple, and hydrogen in white.

tion[12,13,30−38,19,21,22,24−26,28,29] and the activity of antimalarial drugs,[11,25,43−52,30,53−57,32,34,35,39−42] fundamental understanding of the structures and dynamics at both the crystal−solution interface and in the solution bulk, and on their correlation to the crystallization mechanism and the activity of the antimalarials, remains elusive.

Here we focus on the structuring and dynamics of a mixed organic−aqueous solvent near the surfaces of β-hematin using a homogeneous mixture of normal 1-octanol and water as a model. The β-hematin crystals that emerge from these complex media exhibit a rodlike morphology (Figure 1c), commonly exposing to the surrounding solvent distinct (100), (010), and (001) crystallographic faces and, in some crystals, a (011) face. The (100) and (011) faces are topographically smooth and exhibit alternating stripes of exposed polar (carboxyl) and nonpolar (e.g., methyl/methylene) groups (Figure 1d,e). The (001) face exhibits similar stripes (Figure 1f) but is topologically rough with grooves as deep as ~1.0 nm (Figure 1d). The stripes of polar groups on the (001) face lie on ledges inside of the grooves, whereas the bottoms of the grooves and regions protruding from the surface comprise nonpolar groups (Figure 1d). Although the (100), (011), and (001) faces all present stripe-like motifs, the center-to-center spacing between the polar stripes is different (1.5, 1.7, and 1.4 nm, respectively), as is the overall surface density of polar groups (0.85, 1.00, and 1.16 groups per nm^2, respectively). Lastly, the (010) face is topographically rough with periodic indentations ~0.6 nm deep, as measured from the outermost heavy atoms, and it exposes only nonpolar groups.

We explore the properties of a 5 wt % water−octanol mixture; owing to the lower molecular weight of water, the number of water molecules in this mixture is ~28% of the total number of molecules. This solvent composition was chosen to model the majority components in the solution used to precipitate β-hematin in recent experiments.[29,26,36,37,45−50]

METHODS

We employed molecular dynamics (MD) simulations conducted with GROMACS 5.1.5.[58] The simulations were performed using the AMBER-based (FF99SBILDN[59]) force field developed by Becker et al.[60] for β-hematin, the TIP3P model of water,[61] and an all-atom representation of n-octanol based on the generalized AMBER force field (GAFF).[62] The equations of motion in all simulations were integrated using the leapfrog algorithm with a 2 fs time step, employing the LINCS[63] method to restrain bond lengths between heavy and

https://doi.org/10.1021/acs.jpcb.1c06589
J. Phys. Chem. B 2021, 125, 11264−11274

hydrogen atoms and the SETTLE[64] algorithm to model water molecules as rigid bodies. Interactions were computed using a 1 nm cutoff and periodic boundary conditions in all three directions of the simulation cell. Long-range contributions to electrostatic interactions were handled with the particle mesh Ewald method[65] using an error tolerance of 10^{-5}.

The crystal structure data for the β-hematin unit cell was taken from the Cambridge Structural Database (REFCODE AYILIE[66,67]). Models of the crystallographic surfaces were created by replicating the unit cell to create supercells. For the (100), (010), and (001) surfaces, 3 × 3 × 5, 4 × 3 × 4, and 3 × 3 × 4 supercells were generated, respectively; for the (011) surface a 3 × 3 × 9 supercell was generated by cleaving a larger 3 × 12 × 14 structure along the (011) plane. Each supercell was rotated to align the normal vector for the face of interest along the z-axis of the simulation cell, modifying the angles of the triclinic box as needed to preserve the periodicity of the structure. The simulation cell was then enlarged along the z-axis to create an infinite crystal slab with two exposed surfaces (Figure 1h). To minimize finite size effects, the z-dimension of the simulation cell was chosen to be at least 3 times the thickness of the crystal slab. The vacuum space above and below the crystal slab was then solvated with a 5 wt % water in n-octanol mixture (Figure 1h).

The energy of solvated systems was minimized with the steepest decent algorithm to remove forces of >1000 kJ mol^{-1} nm^{-1} on atoms. Each system was subsequently equilibrated for 10 ns in the NVT ensemble at 325 K using a Bussi–Parrinello thermostat[68] with a 0.1 ps time constant and then run for an additional 220 ns at 325 K and 1 bar in the NP_zT ensemble, saving trajectory information from the last 200 ns for analysis. Constant pressure (isostress) conditions normal to the surface were maintained during the NP_zT simulations by applying a Parrinello–Rahman barostat[69] with a 2 ps time constant along the z-direction of the simulation cell; no pressure coupling was applied in the x- and y-directions.

RESULTS AND DISCUSSION

To characterize the solvent structure near the faces of β-hematin, we computed the density profiles for n-octanol along the z-direction of the simulation cell (Figure 2a). The position of the outermost exposed heavy atom was used to define the z = 0 origin for each surface. This arbitrary choice leads to nonzero densities for z < 0 due to solvent penetration into surface corrugations but nonetheless facilitates straightforward comparison between different faces of β-hematin. The oscillations in the profiles near the solid–liquid interfaces (z < 1 nm) reflect local density inhomogeneities arising from structuring of the solvent into layers. The decay of the oscillations as z increases signifies that the layers become more diffusive further away from the surface, until they eventually vanish at $z \approx 1.5$ nm where the solvent recovers bulk-like properties.

Solvent layering near solid surfaces is a ubiquitous phenomenon that has been studied extensively, predominantly in aqueous solutions, using experiment[70−73] and computer simulation.[47,74,73,75] Layering occurs even in systems with purely repulsive fluid–wall interactions but is often enhanced by attraction.[76] Accordingly, density oscillations are strong near (100), (011), and (001) faces, which contain polar groups that can form H-bonds with the solvent species but are nearly absent near the apolar (010) surface (Figure 2a). The primary peak associated with the solvent contact layer, however, is most

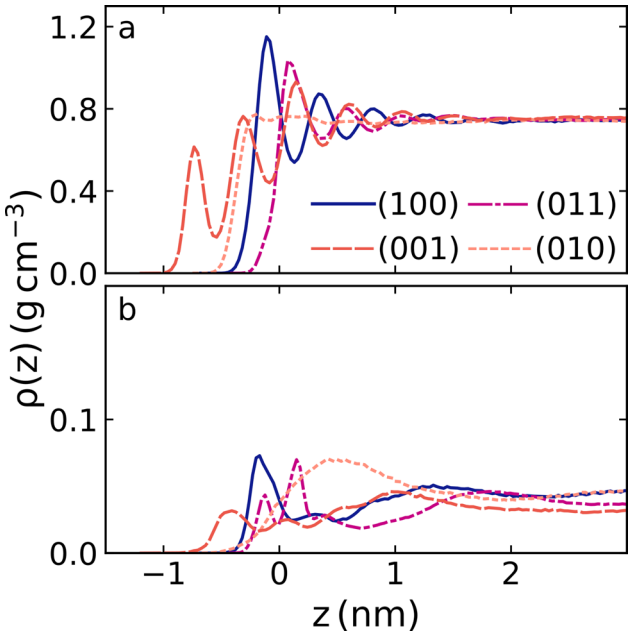

Figure 2. Solvent density profiles. Density profiles for n-octanol (a) and water (b) as functions of distance z from the (100), (011), (001), and (010) faces of β-hematin. The z = 0 origin is defined by the position of the outermost exposed heavy atoms on each face.

pronounced for the (100) surface, which has a lower areal density of polar groups than the (011) and (001) faces, indicating that other factors besides surface chemistry (e.g., surface roughness) also influence structuring near the interface. Indeed, the density profile for the highly corrugated (001) surface exhibits three large oscillations of similar magnitude rather than a single, well-defined contact peak, as observed for the relatively flat (100) and (011) faces.

Density profiles for water were also analyzed near the surfaces (Figure 2b). Similar to those for n-octanol, the water density profiles for the three faces with exposed polar groups exhibit pronounced contact peaks, whereas a more diffusive first peak is observed for the (010) surface. For n-octanol, however, the peaks in the density profiles for the (100), (011), and (001) surfaces are regularly spaced and ∼0.5 nm in width, consistent with the formation of multiple solvation layers. For water, by contrast, density oscillations beyond the contact peak are irregular and diffuse, indicating the presence of large inhomogeneities.

Inspection of the simulation trajectories revealed that these large density inhomogeneities are associated with aggregates of H-bonded species (Figure 3) and contain water and n-octanol; the aggregates near the crystal surface also incorporate hematin carboxyl groups. To characterize these aggregates, we computed the size distribution of H-bonded clusters. Standard geometric criteria based on the donor–acceptor distance and angle were used to identify H-bonds,[77] and pairs of H-bonded species were considered to be part of the same cluster. The aggregation number N_{agg} was defined as the number of oxygen atoms in the cluster, and the location of each cluster was determined from its geometric center computed using the positions of the oxygen atoms. Clusters located within 1 nm of each surface were considered to be in the interfacial region. For comparison, a similar analysis was also performed for a bulk water in n-octanol mixture with the same composition.

https://doi.org/10.1021/acs.jpcb.1c06589
J. Phys. Chem. B 2021, 125, 11264−11274

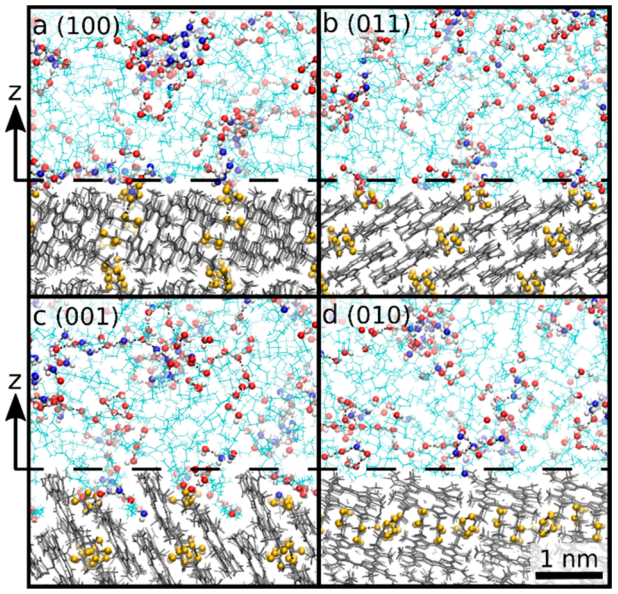

Figure 3. Schematic presentations of the solvent structures and H-bonded clusters near the surfaces of β-hematin. (a, b, c, d) Side views of the (100), (011), (001), and (010) faces of β-hematin, respectively. The dashed line in each panel indicates the position of the outermost heavy atom defining the origin at $z = 0$. Hematin (gray) and *n*-octanol (cyan) are displayed using stick representations. The hydrogen atoms of water and the *n*-octanol hydroxyl group are shown as white spheres, whereas the oxygens of heme, *n*-octanol, and water are shown as gold, red, and blue spheres, respectively.

For the bulk mixture, the distribution of aggregate sizes is broad and nearly flat, exhibiting a weak peak around 5 O atoms (Figure 4a). This result is quantitatively consistent with prior computational studies of water in *n*-octanol mixtures.[78,79] Detailed analyses in these studies have demonstrated that the broadness of the distribution arises from a diverse spectrum of H-bonded aggregates with a large variation in size and shape. The architecture of the aggregates is also diverse, ranging from linear chain-like aggregates formed through the H-bonding of hydroxyl heads of *n*-octanol molecules to water-centered micellar aggregates. The aggregate size distribution near the (010) face of β-hematin is remarkably similar to that in the bulk mixture (Figure 4e), whereas the distributions near the (100), (011), and (001) faces qualitatively differ and exhibit substantially lower numbers of large clusters (Figure 4b–d). These observations suggest that the strong layering near the (100), (011), and (001) faces may disrupt the H-bond network of the solvent, resulting in small aggregates that interact with exposed polar groups on these surfaces.

The density profiles and cluster analysis reveal that the structure of the solvent is strongly perturbed near the faces of β-hematin with exposed polar groups. To further investigate the structure in the interfacial regions, we analyzed the orientational ordering of *n*-octanol by computing the joint distribution $P(\cos(\theta),z_{COM})$, where θ is the angle between the surface normal and the vector adjoining *n*-octanol's tail carbon and oxygen atom and z_{COM} is the normal component of the vector between *n*-octanol's center-of-mass (COM) and the outermost heavy atom on the crystal face. Thus, $\cos(\theta) = \{1,-1\}$ corresponds to orientations in which *n*-octanol is perpendicular to the surface with its hydroxyl group facing toward and away from the surface, respectively, and $\cos(\theta) = 0$ indicates an orientation parallel to the crystal face (Figure 5a).

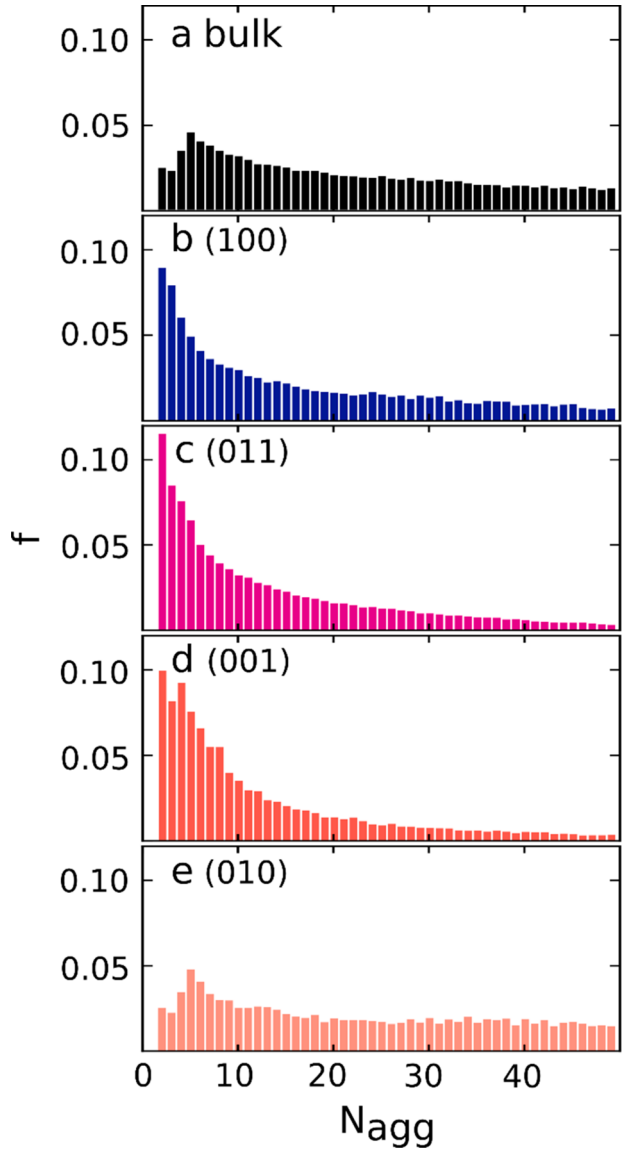

Figure 4. Fraction of all oxygen atoms in H-bonded clusters with aggregation number N_{agg}. (a) Distribution in a bulk water-octanol mixture. (b, c, d, e) Cluster distributions computed within 1 nm of the (100), (011), (001), and (010) faces of β-hematin, respectively. Standard geometric criteria based on the donor–acceptor distance and angle were used to identify H-bonds[77] between water, *n*-octanol, and carboxyl groups on the crystal surface, and pairs of H-bonded species were defined as parts of the same cluster.

Heatmaps of $P(\cos(\theta),z_{COM})$ for the (100) and (011) faces show local maxima near $z_{COM} = 0$ nm and $\cos(\theta) = 0$, which reveal that *n*-octanol preferentially orients parallel to the surface in the contact layer (Figure 5b,c). More diffuse peaks are observed for $0 < \cos(\theta) < 1$ at this distance, suggesting that a smaller fraction of the molecules adopt perpendicular orientations with their hydroxyls pointed toward the surface. Preferential parallel ordering also occurs in the second layers near these two surfaces, but the minority population assumes orientations opposite to those in the first layer (i.e., $-1 < \cos(\theta) < 0$). Although parallel orientations are dominant near the surface, this behavior suggests that a small fraction of the molecules in the first two layers may form lamellar-like structures.

https://doi.org/10.1021/acs.jpcb.1c06589
J. Phys. Chem. B 2021, 125, 11264–11274

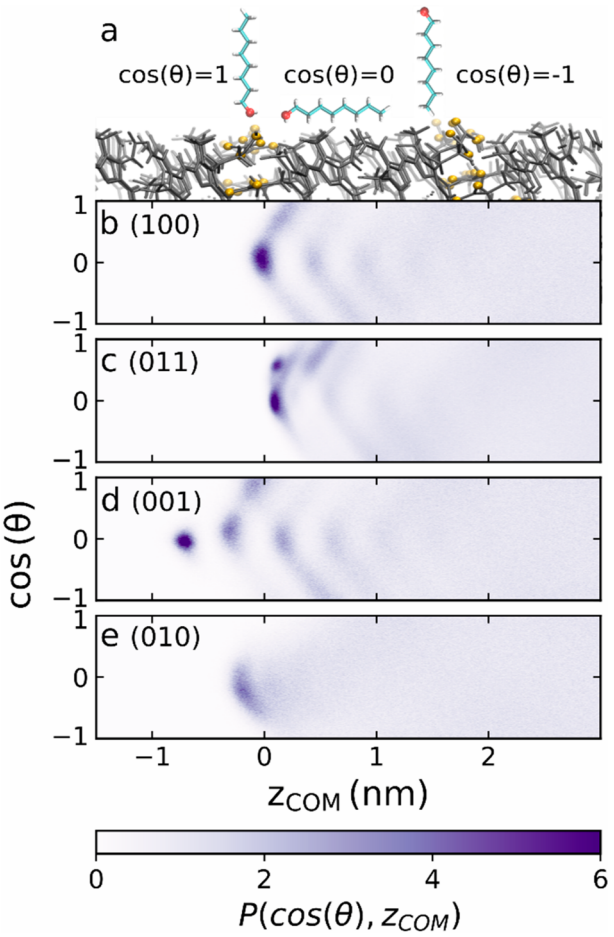

Figure 5. Orientational distributions of *n*-octanol. (a) Schematic illustration of the orientations of *n*-octanol relative to the surface and the corresponding values of cos(θ). The oxygen atoms in hematin are shown as gold spheres, whereas all other atoms in the crystal are shown using gray sticks. Atom coloring for *n*-octanol is carbon (cyan), hydrogen (white), and oxygen (red). (b, c, d, e) Heatmaps of the $P(\cos(\theta), z_{COM})$ distributions for the (100), (011), (001), and (010) faces of β-hematin, respectively, where z_{COM} is the distance from the surface of the center of mass of *n*-octanol. The $P(\cos(\theta), z_{COM})$ distributions are normalized so that they approach unity as bulk-like behavior is recovered far away from the surfaces (i.e., $P(\cos(\theta), z_{COM} \to \infty) \to 1$).

As suggested by the density profiles (Figure 2), corrugations on the (001) face lead to more complex structuring near this surface. The strongest maxima in the $P(\cos(\theta), z_{COM})$ heatmap for this surface is located at $z_{COM} \approx -0.8$ nm and cos(θ) = 0 and arise from *n*-octanol molecules that adsorb into the grooves on this face (Figures 5d and 3c). The two regions of intensity at $z_{COM} \approx -0.3$ nm correspond to molecules adsorbed on the ledges inside the grooves. Whereas some molecules adopt parallel conformations (cos(θ) = 0), others orient with their hydroxyl groups pointed toward the surface to interact with the exposed polar groups on the ledges (cos(θ) ≈ 0.9). The third, less distinct feature at $z_{COM} \approx 0.4$ nm and $-1 < \cos(\theta) < 0$ is associated with interaction of *n*-octanol with the protrusions that comprise nonpolar groups. Lastly, in contrast with the other three surfaces, orientational ordering near the (010) face is relatively weak and decays much more rapidly as a function of z_{COM} (Figure 5e), consistent with the absence of strong translational ordering near this surface (Figure 2a). At the interface, however, *n*-octanol molecules preferentially adopt tilted orientations in which their alkyl tails are closer than their hydroxyl groups to the surface (Figure 5e).

The strong influence of surface chemistry and topology on solvent structure can also be seen in heatmaps of $P_{OH}(x,z)$, the distribution of *n*-octanol hydroxyl groups in the *xz* plane perpendicular to the surface (Figure 6). The $P_{OH}(x,z)$ distributions demonstrate that *n*-octanol hydroxyl groups are spatially localized around surface carboxyls. Spatial heterogeneities are also observed in the in-plane hydroxyl distribution, $P_{OH}(x,y)_{z^*}$, computed in the vicinity of each surface (Figure 7). The degree of localization is greatest for the (011) surface because it exposes adjacent pairs of carboxyl groups that slightly protrude from the surface and form 0.9 ± 0.1 H-bonds per carboxyl on average with the solvent. Similarly, the (001) surface presents adjacent pairs of carboxyl groups, but they reside on ledges inside surface grooves. Steric interactions inside the grooves slightly hinder H-bond formation, reducing the number of H-bonds per carboxyl to 0.7 ± 0.1 and hence the degree of hydroxyl localization compared to the (011) face. Lastly, the carboxyl groups on the (100) face form 0.8 ± 0.1 H-bonds per carboxyl with the solvent, but their isolated nature results in reduced hydroxyl localization compared to the (011) face.

Owing to the absence of exposed polar groups on the (010) surface, the $P_{OH}(x,z)$ distribution for this face is more uniform than for the other surfaces (Figure 6d). Interestingly, however, the heatmap of $P_{OH}(x,y)_{z^*}$ reveals the hydroxyl groups of *n*-octanol molecules are also spatially localized on this surface (Figure 7d). The density and orientational distributions suggest that *n*-octanol forms a diffusive contact layer in which the molecules are oriented with their alkyl tail groups tilted toward the surface (Figures 2 and 5). This tilt allows *n*-octanol molecules to sit with their alkyl tails in shallow grooves on this surface and their hydroxyl groups exposed. Moreover, regular spaced regions of intensity in the $P_{OH}(x,y)_{z^*}$ distribution indicate that the molecules also preferentially orient in the *xy* plane parallel to the surface to bring the hydroxyl head groups of neighboring molecules into close proximity to facilitate H-bonding.

The spatial distributions of the *n*-octanol and water in the vicinity of the β-hematin crystal faces suggest that surface chemistry and topology strongly affect the ordering of the solvent at the interface. To understand their influence on solvent dynamics, we computed the normalized survival-time correlation function[80] for *n*-octanol molecules in the different solvent layers near each surface,

$$C_R(t) = \frac{1}{N_O} \sum_{j=1}^{N_O} \frac{\langle p_{R,j}(0) p_{R,j}(t) \rangle}{p_{R,j}(0)^2} \quad (1)$$

where N_O is the number of the *n*-octanol molecules and $p_{R,j}(t)$ is an indicator function, which is 1 when the center-of-mass of molecule *j* remains in the layer for observation time *t* and 0 otherwise. We computed $C_R(t)$ in three slabs parallel to each surface, using a slab width of 0.5 nm in the *z*-direction. For the (100), (011), and (001) faces, the slabs were centered on the positions of the first three peaks in the density profiles (Figure 2a). For the (010) face, we considered three adjacent slabs due to the absence of well-defined solvent layers near this surface.

As expected, the $C_R(t)$ functions decay monotonically, indicating that the probability that *n*-octanol molecules remain

https://doi.org/10.1021/acs.jpcb.1c06589
J. Phys. Chem. B 2021, 125, 11264−11274

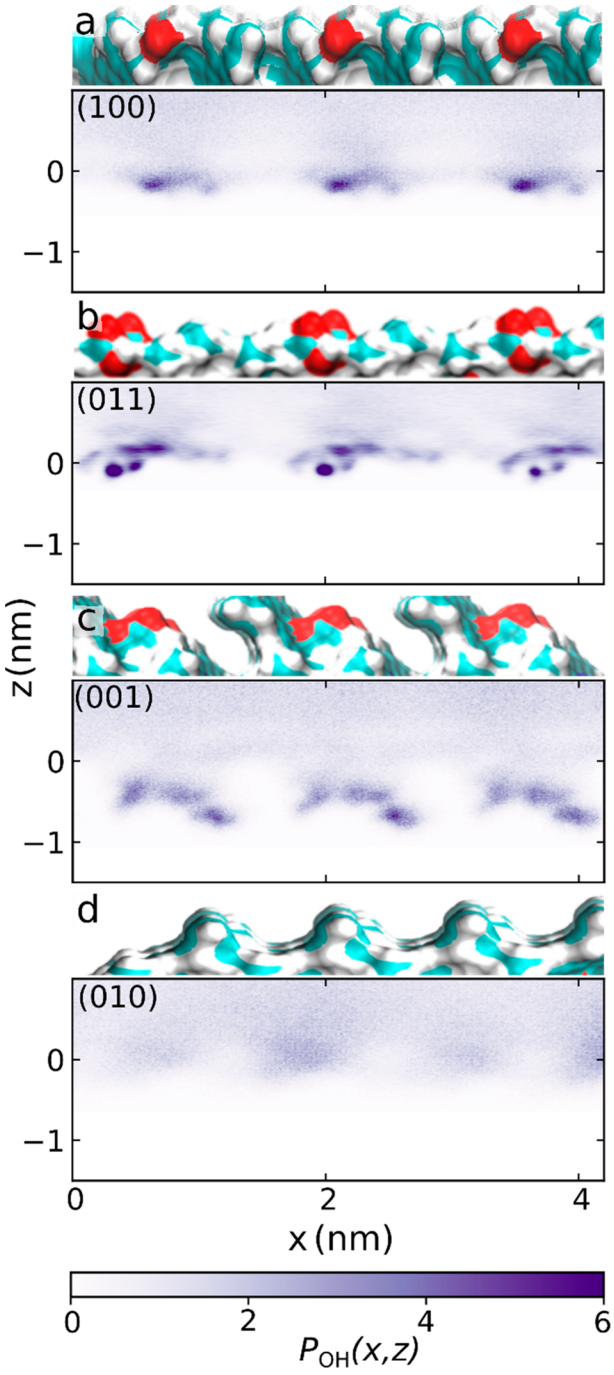

Figure 6. Spatial distributions of the hydroxyl groups of *n*-octanol in the *xz* planes perpendicular to each surface. (a, b, c, d) Heatmaps of the $P_{OH}(x,z)$ for the (100), (011), (001), and (010) faces of *β*-hematin, respectively. The distributions are normalized such that $P_{OH}(x,z\rightarrow\infty) \rightarrow 1$. The panel above each heat map shows a side view of the corresponding surface in the *xz* plane, with oxygen shown in red, nitrogen in blue, carbon in cyan, and hydrogen in white.

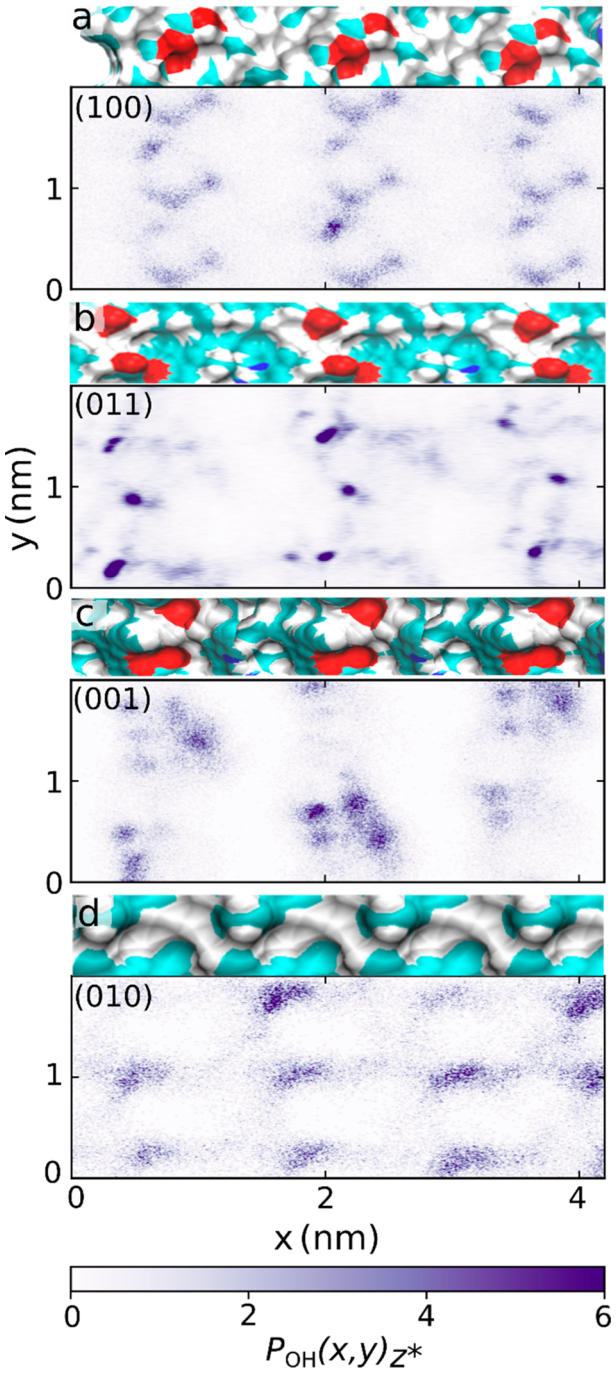

Figure 7. Spatial distributions of the hydroxyl groups of *n*-octanol in the *xy* planes parallel to each surface. (a, b, c, d) Heatmaps of the $P_{OH}(x,y)_{z^*}$ for the (100), (011), (001), and (010) faces of *β*-hematin, respectively. The distributions are averaged over a 0.5 nm slab along the *z*-axis centered on the position z^* and normalized such that $P_{OH}(x,y)_{z^*\rightarrow\infty} \rightarrow 1$. For the (100), (011), and (001) faces, the positions of the surface polar groups were used to define z^*, whereas the position of the contact layer was used for the (010) face due to the absence of polar groups on this surface. The panel above each heat map shows a top view of the corresponding surface in the *xy* plane, with oxygen shown in red, nitrogen in blue, carbon in cyan, and hydrogen in white.

in a given solvent layer decreases as the observation time increases (Figure 8). In each case, the decay of $C_R(t)$ is well-described by a linear combination of two stretched exponential functions, $C_R^{fit}(t) = Ae^{-(t/\tau_f)^{\beta f}} + (1-A)e^{-(t/\tau_s)^{\beta s}}$. This functional form has been employed in previous studies,[80,81] and it is physically motivated by a two-step relaxation process. The first term captures fast modes associated with local vibrations of molecules on short time scales when their motions are confined by surrounding neighbors and/or the crystal surface. On these short time scales, molecules near slab boundaries will vibrate in and out of the slabs, resulting in rapid initial decay of $C_R(t)$. The second term, by contrast, captures slower processes

https://doi.org/10.1021/acs.jpcb.1c06589
J. Phys. Chem. B 2021, 125, 11264−11274

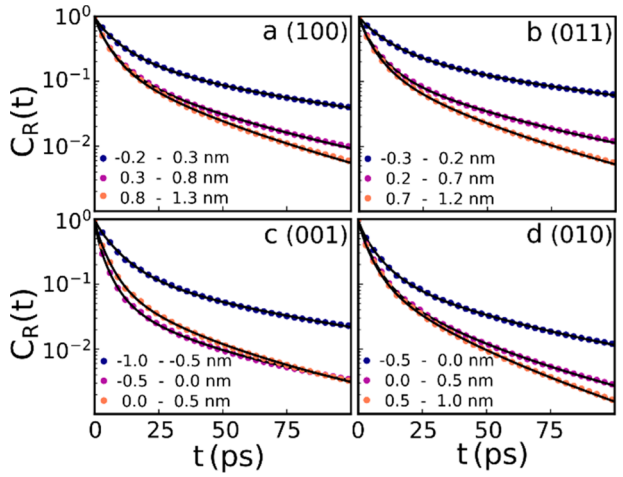

Figure 8. Survival-time correlation functions for *n*-octanol molecules in different solvation layers. (a, b, c, d) Correlation functions $C_R(t)$ for *n*-octanol molecules in different solvation layers near the (100), (011), (001), and (010) faces of *β*-hematin, respectively. Simulation data (dotted lines) for different layers are shown in different colors: first layer (blue), second (purple), and third (orange); the ranges of *z* values used to define the layers are listed in the panel legends. Black lines are fits of the simulation data to $C_R^{fit}(t) = Ae^{-(t/\tau_f)^{\beta_f}} + (1-A)e^{-(t/\tau_s)^{\beta_s}}$.

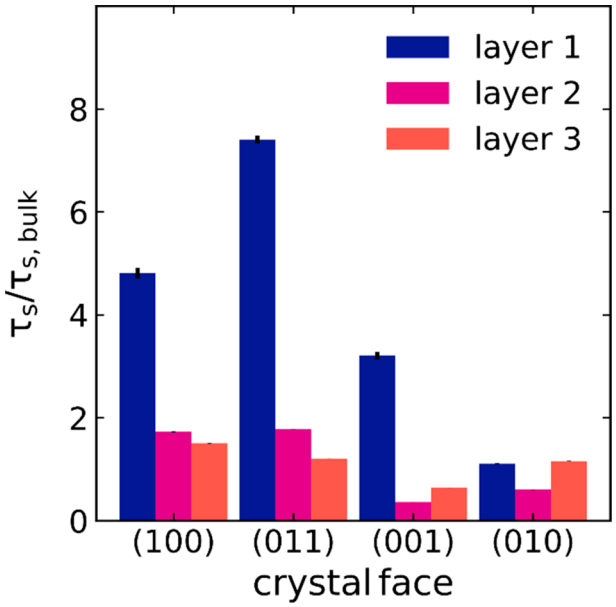

Figure 9. Normalized survival times for different solvation layers. Survival times τ_s for different layers extracted from the stretched exponential fits to the correlation functions in Figure 8, normalized by the bulk value $\tau_{s,bulk} \approx 8.1$ ps computed using a 0.5 nm slab far away (≈4 nm) from the interface.

associated with escape from the solvent layers. As noted previously, this behavior is reminiscent of two-step cage rattling and breaking relaxation mechanisms in bulk supercooled liquids.[82,83] Details of the fitting procedures are described in Supporting Information.

The time constant associated with the slower modes, τ_s, characterizes the relaxation of each solvent layer and hence is the primary quantity of interest. The values of τ_s extracted from the $C_R^{fit}(t)$ fits are conveniently normalized by the relaxation time $\tau_{s,bulk} \approx 8.1$ ps computed in a slab in a bulk water in *n*-octanol mixture. The normalized time constant $\tau_s/\tau_{s,bulk}$ is largest for the first solvent layers, indicating that the relaxations are slower near each surface due to confinement effects and interactions with polar surface groups (Figure 9). Consistent with this interpretation, the longest relaxation times are observed for the first solvent layers near the (100) and (011) faces, in which *n*-octanol molecules exhibit strong translational and orientational ordering and localization near exposed carboxyl groups. For these two faces, which are relatively flat, $\tau_s/\tau_{s,bulk}$ monotonically decreases with increasing layer number due to decay of structural order in the solvent further away from the surfaces, recovering bulk-like dynamics in the third layer. For the (001) and (010) faces, by contrast, $\tau_s/\tau_{s,bulk}$ is smallest in the second layer and below the value of 1 expected in the bulk. Although the precise mechanism for the faster-than-bulk dynamics in these layers remains unknown, we hypothesize that solvent relaxation may be facilitated by the presence of surface corrugations. Indeed, τ_s is also below the bulk value in the third layer near the (001) face, which has large surface corrugations that protrude into this region. Hence, the relaxation dynamics appear to be strongly affected by surface chemistry and topology and the influence that these features have on the local ordering in the solvent.

CONCLUSIONS AND IMPLICATIONS

We performed molecular dynamics simulations to study the structure and dynamics of solvent near the (100), (011), (001), and (010) faces of *β*-hematin. The model solvent contained 5 wt % water added to *n*-octanol and mimicked the dominant constituents of the solvent used in recent experiments aimed to elucidate the mechanisms of *β*-hematin crystallization. The octanol mixture, in turn, was formulated to mimic the lipid structures in the digestive vacuole of malaria parasites that host hematin crystallization *in vivo*.

The simulations revealed that the properties of the solvent in the layer adjacent to the crystal are strongly affected by the distinct chemical and topological features presented by each crystal face. Polar stripes on the (100), (011), and (001) surfaces consisting of exposed carboxyl groups promote organization of the solvent into at least three distinct layers that disrupt the H-bond network within the ∼1 nm interfacial region extending from each surface. Near the flat (100) and (011) surfaces, the degree of ordering is most pronounced in the contact layers in which *n*-octanol molecules preferentially lie flat against the surfaces and orient within the plane to form H-bonds with the exposed carboxyl groups and bring their alkyl tails into close proximity with apolar surface moieties. Corrugations on the (001) face result in more complex structuring in the contact layer in which *n*-octanol molecules adopt both parallel and tilted orientations with respect to the surface to facilitate H-bonding with exposed carboxyl groups that reside atop ledges inside the surface grooves. Near the apolar (010) face the structural ordering is comparatively short-ranged and diffusive. Still, *n*-octanol molecules were still found to preferentially orient in the planes perpendicular and parallel to the interface to allow their alkyl tails to interact with shallow apolar surface grooves and promote H-bonding between solvent species.

Lastly, our simulations demonstrated that structuring of the solvent near the different faces of *β*-hematin leads to distinct

https://doi.org/10.1021/acs.jpcb.1c06589
J. Phys. Chem. B 2021, 125, 11264−11274

interfacial dynamics. The relaxation time of *n*-octanol molecules is longest in the contact layers and appears to correlate with the degree of structural ordering. Near the (100) and (011) faces, the relaxation time decreases monotonically with the distance from the surface, recovering bulk-like dynamics in the third solvation layer. Near the (001) and (010) faces, by contrast, the decrease is nonmonotonic, and anomalous faster-than-bulk relaxation dynamics are observed in the second solvation layer. We posit that this unusual behavior may arise from the presence of corrugations on these faces, but the influence of surface roughness on solvent dynamics remains incompletely understood and an interesting avenue for future investigation.

These findings illuminate fundamental features of the mechanisms of hematin crystallization and its inhibition by antimalarials. The hydrogen-bonded water clusters extant in the solution bulk and overexpressed in the vicinity of the crystal surfaces stabilize ionic groups that reside in them owing to the high dielectric constant of water. Stable deprotonated carboxyls, COO^-, are essential for the formation of the coordination Fe−OOC bond that upholds β-hematin and hemozoin crystals. Furthermore, quinoline antimalarial drugs incorporate tertiary amines that may protonate to positive ions, whereas artemisinins carry carboxyl groups that may dissociate and acquire negative charge. Stabilizing both positive and negative ions activates Coulomb forces with similar molecules or with hematin and the crystal surface moieties.

β-Hematin and hemozoin crystals are elongated along their z axes due to fast growth in the [001] direction (Figure 1c). This face exhibits weaker solvent structuring and faster solvent dynamics (Figures 5−9), both due to the weaker interactions of the solvent with the exposed hematin residues. Solute−solvent bond strength has been implicated to dictate the activation barrier for solute incorporation into crystals, which involves partial stripping of the solvent molecules that enshroud the growth sites on the crystal surface.[84−86] In addition, solvent dynamics prescribes the rate of ingress of solute into the growth sites. Thus, the distinct solvent structuring and dynamics on the anisotropic crystal faces may be a part of the mechanism that regulates the crystal habit.

The solvent structuring provides a direct example of the impact of the crystal surface on the structure and dynamics of the solvent in nonaqueous environments. Importantly, our findings demonstrate that solvent structuring may be upheld by bonds distinct from the hydrogen bonds, as on the apolar (010) face, and may be a general feature of all solvents in contact with periodic crystal surfaces. The slow solvent dynamics in the vicinity of the crystal faces retards the diffusion of hematin molecules along the surface en route to their incorporation sites[29,36,37] and suggests a pathway to control hematin crystallization using additives that disrupt or reinforce solvent structures.

■ ASSOCIATED CONTENT

Supporting Information

The Supporting Information is available free of charge at https://pubs.acs.org/doi/10.1021/acs.jpcb.1c06589.

Description of models for the survival time correlation functions and numerical fitting procedures; tables of optimal fit parameters (PDF)

■ AUTHOR INFORMATION

Corresponding Authors

Peter G. Vekilov − *William A. Brookshire Department of Chemical and Biomolecular Engineering and Department of Chemistry, University of Houston, Houston, Texas 77204, United States;* orcid.org/0000-0002-3424-8720; Email: vekilov@uh.edu

Jeremy C. Palmer − *William A. Brookshire Department of Chemical and Biomolecular Engineering, University of Houston, Houston, Texas 77204, United States;* Email: jcpalmer@uh.edu

Author

Laksmanji Verma − *William A. Brookshire Department of Chemical and Biomolecular Engineering, University of Houston, Houston, Texas 77204, United States*

Complete contact information is available at: https://pubs.acs.org/10.1021/acs.jpcb.1c06589

Notes

The authors declare no competing financial interest.

■ ACKNOWLEDGMENTS

This work was supported by NIH (Award AI150763), the National Science Foundation (Award DMR-2128121), and The Welch Foundation (Grant E-1882). Computational resources were provided by the Hewlett-Packard Enterprise Data Science Institute and the University of Houston and the Texas Advanced Computing Center at the University of Texas at Austin.

■ REFERENCES

(1) Goldberg, D. E.; Slater, A. F.; Cerami, A.; Henderson, G. B. Hemoglobin Degradation in the Malaria Parasite Plasmodium Falciparum: An Ordered Process in a Unique Organelle. *Proc. Natl. Acad. Sci. U. S. A.* **1990**, *87* (8), 2931−2935.

(2) Eastman, R. T.; Fidock, D. A. Artemisinin-Based Combination Therapies: A Vital Tool in Efforts to Eliminate Malaria. *Nat. Rev. Microbiol.* **2009**, *7* (12), 864−874.

(3) Banerjee, R.; Liu, J.; Beatty, W.; Pelosof, L.; Klemba, M.; Goldberg, D. E. Four Plasmepsins Are Active in the Plasmodium Falciparum Food Vacuole, Including a Protease with an Active-Site Histidine. *Proc. Natl. Acad. Sci. U. S. A.* **2002**, *99* (2), 990−995.

(4) Gamboa de Dominguez, N. D.; Rosenthal, P. J. Cysteine Proteinase Inhibitors Block Early Steps in Hemoglobin Degradation by Cultured Malaria Parasites. *Blood* **1996**, *87* (10), 4448−4454.

(5) Orjih, A. U.; Banyal, H. S.; Chevli, R.; Fitch, C. D. Hemin Lyses Malaria Parasites. *Science (Washington, DC, U. S.)* **1981**, *214* (4521), 667−669.

(6) Loria, P.; Miller, S.; Foley, M.; Tilley, L. Inhibition of the Peroxidative Degradation of Haem as the Basis of Action of Chloroquine and Other Quinoline Antimalarials. *Biochem. J.* **1999**, *339* (2), 363−370.

(7) Fitch, C. D.; Chevli, R.; Kanjananggulpan, P.; Dutta, P.; Chevli, K.; Chou, A. C. Intracellular Ferriprotoporphyrin IX Is a Lytic Agent. *Blood* **1983**, *62* (6), 1165−1168.

(8) Ridley, R. G. Medical Need, Scientific Opportunity and the Drive for Antimalarial Drugs. *Nature* **2002**, *415* (6872), 686−693.

(9) Pagola, S.; Stephens, P. W.; Bohle, D. S.; Kosar, A. D.; Madsen, S. K. The Structure of Malaria Pigment β-Haematin. *Nature* **2000**, *404* (6775), 307−310.

(10) Kapishnikov, S.; Berthing, T.; Hviid, L.; Dierolf, M.; Menzel, A.; Pfeiffer, F.; Als-Nielsen, J.; Leiserowitz, L. Aligned Hemozoin Crystals in Curved Clusters in Malarial Red Blood Cells Revealed by

Nanoprobe X-Ray Fe Fluorescence and Diffraction. *Proc. Natl. Acad. Sci. U. S. A.* **2012**, *109* (28), 11184−11187.
(11) Gorka, A. P.; de Dios, A.; Roepe, P. D. Quinoline Drug−Heme Interactions and Implications for Antimalarial Cytostatic versus Cytocidal Activities. *J. Med. Chem.* **2013**, *56* (13), 5231−5246.
(12) Francis, S. E.; Sullivan, D. J.; Goldberg, D. E. Hemoglobin Metabolism in the Malaria Parasite Plasmodium Falciparum. *Annu. Rev. Microbiol.* **1997**, *51*, 97−123.
(13) de Villiers, K. A.; Osipova, M.; Mabotha, T. E.; Solomonov, I.; Feldman, Y.; Kjaer, K.; Weissbuch, I.; Egan, T. J.; Leiserowitz, L. Oriented Nucleation of Beta-Hematin Crystals Induced at Various Interfaces: Relevance to Hemozoin Formation. *Cryst. Growth Des.* **2009**, *9* (1), 626−632.
(14) Kapishnikov, S.; Staalsø, T.; Yang, Y.; Lee, J.; Pérez-Berná, A. J.; Pereiro, E.; Yang, Y.; Werner, S.; Guttmann, P.; Leiserowitz, L.; Als-Nielsen, J. Mode of Action of Quinoline Antimalarial Drugs in Red Blood Cells Infected by *Plasmodium falciparum* Revealed in Vivo. *Proc. Natl. Acad. Sci. U. S. A.* **2019**, *116* (46), 22946−22952.
(15) Kapishnikov, S.; Grolimund, D.; Schneider, G.; Pereiro, E.; McNally, J. G.; Als-Nielsen, J.; Leiserowitz, L. Unraveling Heme Detoxification in the Malaria Parasite by in Situ Correlative X-Ray Fluorescence Microscopy and Soft X-Ray Tomography. *Sci. Rep.* **2017**, *7*, 7610.
(16) Kapishnikov, S.; Weiner, A.; Shimoni, E.; Schneider, G.; Elbaum, M.; Leiserowitz, L. Digestive Vacuole Membrane in Plasmodium Falciparum-Infected Erythrocytes: Relevance to Templated Nucleation of Hemozoin. *Langmuir* **2013**, *29* (47), 14595−14602.
(17) Kapishnikov, S.; Hempelmann, E.; Elbaum, M.; Als-Nielsen, J.; Leiserowitz, L. Malaria Pigment Crystals: The Achilles' Heel of the Malaria Parasite. *ChemMedChem* **2021**, *16*, 1515−1532.
(18) Kapishnikov, S.; Leiserowitz, L.; Yang, Y.; Cloetens, P.; Pereiro, E.; Awamu Ndonglack, F.; Matuschewski, K.; Als-Nielsen, J. Biochemistry of Malaria Parasite Infected Red Blood Cells by X-Ray Microscopy. *Sci. Rep.* **2017**, *7*, 802.
(19) Noland, G. S.; Briones, N.; Sullivan, D. J., Jr The Shape and Size of Hemozoin Crystals Distinguishes Diverse Plasmodium Species. *Mol. Biochem. Parasitol.* **2003**, *130* (2), 91−99.
(20) Kapishnikov, S.; Weiner, A.; Shimoni, E.; Guttmann, P.; Schneider, G.; Dahan-Pasternak, N.; Dzikowski, R.; Leiserowitz, L.; Elbaum, M. Oriented Nucleation of Hemozoin at the Digestive Vacuole Membrane in Plasmodium Falciparum. *Proc. Natl. Acad. Sci. U. S. A.* **2012**, *109* (28), 11188−11193.
(21) Pisciotta, J. M.; Coppens, I.; Tripathi, A. K.; Scholl, P. F.; Shuman, J.; Bajad, S.; Shulaev, V.; Sullivan, D. J. The Role of Neutral Lipid Nanospheres in Plasmodium Falciparum Haem Crystallization. *Biochem. J.* **2007**, *402*, 197−204.
(22) Hoang, A. N.; Sandlin, R. D.; Omar, A.; Egan, T. J.; Wright, D. W. The Neutral Lipid Composition Present in the Digestive Vacuole of Plasmodium Falciparum Concentrates Heme and Mediates Beta-Hematin Formation with an Unusually Low Activation Energy. *Biochemistry* **2010**, *49* (47), 10107−10116.
(23) Ketchum, M. A.; Olafson, K. N.; Petrova, E. V.; Rimer, J. D.; Vekilov, P. G. Hematin Crystallization from Aqueous and Organic Solvents. *J. Chem. Phys.* **2013**, *139* (12), 121911.
(24) Egan, T. J. Haemozoin Formation. *Mol. Biochem. Parasitol.* **2008**, *157*, 127−136.
(25) Egan, T. J.; Chen, J. Y. J.; de Villiers, K. A.; Mabotha, T. E.; Naidoo, K. J.; Ncokazi, K. K.; Langford, S. J.; McNaughton, D.; Pandiancherri, S.; Wood, B. R. Haemozoin (*β*-Haematin) Biomineralization Occurs by Self-Assembly near the Lipid/Water Interface. *FEBS Lett.* **2006**, *580* (21), 5105−5110.
(26) Vekilov, P. G.; Rimer, J. D.; Olafson, K. N.; Ketchum, M. A. Lipid or Aqueous Medium for Hematin Crystallization? *CrystEngComm* **2015**, *17* (41), 7790−7800.
(27) Weissbuch, I.; Leiserowitz, L. Interplay Between Malaria, Crystalline Hemozoin Formation, and Antimalarial Drug Action and Design. *Chem. Rev.* **2008**, *108* (11), 4899−4914.
(28) Egan, T. J. Recent Advances in Understanding the Mechanism of Hemozoin (Malaria Pigment) Formation. *J. Inorg. Biochem.* **2008**, *102* (5−6), 1288−1299.
(29) Olafson, K. N.; Ketchum, M. A.; Rimer, J. D.; Vekilov, P. G. Molecular Mechanisms of Hematin Crystallization from Organic Solvent. *Cryst. Growth Des.* **2015**, *15*, 5535.
(30) Egan, T. J.; Ross, D. C.; Adams, P. A. Quinoline Antimalarial-Drugs Inhibit Spontaneous Formation of Beta-Hematin (Malaria Pigment). *FEBS Lett.* **1994**, *352* (1), 54−57.
(31) de Villiers, K. A.; Kaschula, C. H.; Egan, T. J.; Marques, H. M. Speciation and Structure of Ferriprotoporphyrin IX in Aqueous Solution: Spectroscopic and Diffusion Measurements Demonstrate Dimerization, but Not Mu-Oxo Dimer Formation. *JBIC, J. Biol. Inorg. Chem.* **2007**, *12* (1), 101−117.
(32) de Villiers, K. A.; Marques, H. M.; Egan, T. J. The Crystal Structure of Halofantrine-Ferriprotoporphyrin IX and the Mechanism of Action of Arylmethanol Antimalarials. *J. Inorg. Biochem.* **2008**, *102* (8), 1660−1667.
(33) Asher, C.; de Villiers, K. A.; Egan, T. J. Speciation of Ferriprotoporphyrin IX in Aqueous and Mixed Aqueous Solution Is Controlled by Solvent Identity, PH, and Salt Concentration. *Inorg. Chem.* **2009**, *48* (16), 7994−8003.
(34) Sullivan, D. J.; Gluzman, I. Y.; Russell, D. G.; Goldberg, D. E. On the Molecular Mechanism of Chloroquine's Antimalarial Action. *Proc. Natl. Acad. Sci. U. S. A.* **1996**, *93* (21), 11865−11870.
(35) Sullivan, D. J. Theories on Malarial Pigment Formation and Quinoline Action. *Int. J. Parasitol.* **2002**, *32* (13), 1645−1653.
(36) Olafson, K. N.; Rimer, J. D.; Vekilov, P. G. Early Onset of Kinetic Roughening Due to a Finite Step Width in Hematin Crystallization. *Phys. Rev. Lett.* **2017**, *119* (19), 198101.
(37) Olafson, K. N.; Ketchum, M. A.; Rimer, J. D.; Vekilov, P. G. Mechanisms of Hematin Crystallization and Inhibition by the Antimalarial Drug Chloroquine. *Proc. Natl. Acad. Sci. U. S. A.* **2015**, *112* (16), 4946−4951.
(38) Heller, L. E.; Roepe, P. D. Quantification of Free Ferriprotoporphyrin IX Heme and Hemozoin for Artemisinin Sensitive versus Delayed Clearance Phenotype Plasmodium Falciparum Malarial Parasites. *Biochemistry* **2018**, *57* (51), 6927−6934.
(39) Sullivan, D. J.; Matile, H.; Ridley, R. G.; Goldberg, D. E. A Common Mechanism for Blockade of Heme Polymerization by Antimalarial Quinolines. *J. Biol. Chem.* **1998**, *273* (47), 31103−31107.
(40) Chong, C. R.; Sullivan, D. J., Jr Inhibition of Heme Crystal Growth by Antimalarials and Other Compounds: Implications for Drug Discovery. *Biochem. Pharmacol.* **2003**, *66* (11), 2201−2212.
(41) Sullivan, D. J. Quinolines Block Every Step of Malaria Heme Crystal Growth. *Proc. Natl. Acad. Sci. U. S. A.* **2017**, *114* (29), 7483−7485.
(42) Correa Soares, J.; Menezes, D.; Vannier-Santos, M. A.; Ferreira-Pereira, A.; Almeida, G. T.; Venancio, T. M.; Verjovski-Almeida, S.; Zishiri, V. K.; Kuter, D.; Hunter, R.; Egan, T. J.; Oliveira, M. F. Interference with Hemozoin Formation Represents an Important Mechanism of Schistosomicidal Action of Antimalarial Quinoline Methanols. *PLoS Neglected Trop. Dis.* **2009**, *3* (7), e477.
(43) Kuter, D.; Streltsov, V.; Davydova, N.; Venter, G. A.; Naidoo, K. J.; Egan, T. J. Solution Structures of Chloroquine−Ferriheme Complexes Modeled Using MD Simulation and Investigated by EXAFS Spectroscopy. *J. Inorg. Biochem.* **2016**, *154*, 114−125.
(44) de Villiers, K. A.; Egan, T. J. Heme Detoxification in the Malaria Parasite: A Target for Antimalarial Drug Development. *Acc. Chem. Res.* **2021**, *54*, 2649.
(45) Ma, W.; Lutsko, J. F.; Rimer, J. D.; Vekilov, P. G. Antagonistic Cooperativity between Crystal Growth Modifiers. *Nature* **2020**, *577* (7791), 497−501.
(46) Ma, W.; Balta, V. A.; West, R.; Newlin, K. N.; Miljanić, O. Š.; Sullivan, D. J.; Vekilov, P. G.; Rimer, J. D. A Second Mechanism Employed by Artemisinins to Suppress Plasmodium Falciparum Hinges on Inhibition of Hematin Crystallization. *J. Biol. Chem.* **2021**, *296*, 100123.

https://doi.org/10.1021/acs.jpcb.1c06589
J. Phys. Chem. B 2021, 125, 11264−11274

(47) Olafson, K. N.; Clark, R. J.; Vekilov, P. G.; Palmer, J. C.; Rimer, J. D. Structuring of Organic Solvents at Solid Interfaces and Ramifications for Antimalarial Adsorption on β-Hematin Crystals. *ACS Appl. Mater. Interfaces* **2018**, *10*, 29288.
(48) Olafson, K. N.; Nguyen, T. Q.; Vekilov, P. G.; Rimer, J. D. Deconstructing Quinoline-Class Antimalarials to Identify Fundamental Physicochemical Properties of Beta-Hematin Crystal Growth Inhibitors. *Chem. - Eur. J.* **2017**, *23* (55), 13638−13647.
(49) Olafson, K. N.; Nguyen, T. Q.; Rimer, J. D.; Vekilov, P. G. Antimalarials Inhibit Hematin Crystallization by Unique Drug−Surface Site Interactions. *Proc. Natl. Acad. Sci. U. S. A.* **2017**, *114*, 7531.
(50) Ketchum, M. A.; Lee, A. M.; Vekilov, P. G.; Rimer, J. D. Biomimetic Assay for Hematin Crystallization Inhibitors: A New Platform to Screen Antimalarial Drugs. *Cryst. Growth Des.* **2017**, *17* (1), 197−206.
(51) Ursos, L. M. B.; DuBay, K. F.; Roepe, P. D. Antimalarial Drugs Influence the PH Dependent Solubility of Heme via Apparent Nucleation Phenomena. *Mol. Biochem. Parasitol.* **2001**, *112* (1), 11−17.
(52) Dinio, T.; Gorka, A. P.; McGinniss, A.; Roepe, P. D.; Morgan, J. B. Investigating the Activity of Quinine Analogues versus Chloroquine Resistant Plasmodium Falciparum. *Bioorg. Med. Chem.* **2012**, *20* (10), 3292−3297.
(53) Gorka, A. P.; Alumasa, J. N.; Sherlach, K. S.; Jacobs, L. M.; Nickley, K. B.; Brower, J. P.; de Dios, A. C.; Roepe, P. D. Cytostatic versus Cytocidal Activities of Chloroquine Analogues and Inhibition of Hemozoin Crystal Growth. *Antimicrob. Agents Chemother.* **2013**, *57* (1), 356−364.
(54) Gorka, A. P.; Jacobs, L. M.; Roepe, P. D. Cytostatic versus Cytocidal Profiling of Quinoline Drug Combinations via Modified Fixed-Ratio Isobologram Analysis. *Malar. J.* **2013**, *12*, 332.
(55) Sherlach, K. S.; Roepe, P. D. Determination of the Cytostatic and Cytocidal Activities of Antimalarial Compounds and Their Combination Interactions. *Curr. Protoc. Chem. Biol.* **2014**, *6* (4), 237−248.
(56) Heller, L. E.; Goggins, E.; Roepe, P. D. Dihydroartemisinin−Ferriprotoporphyrin IX Adduct Abundance in Plasmodium Falciparum Malarial Parasites and the Relationship to Emerging Artemisinin Resistance. *Biochemistry* **2018**, *57* (51), 6935−6945.
(57) Mott, B. T.; Eastman, R. T.; Guha, R.; Sherlach, K. S.; Siriwardana, A.; Shinn, P.; McKnight, C.; Michael, S.; Lacerda-Queiroz, N.; Patel, P. R.; Khine, P.; Sun, H.; Kasbekar, M.; Aghdam, N.; Fontaine, S. D.; Liu, D.; Mierzwa, T.; Mathews-Griner, L. A.; Ferrer, M.; Renslo, A. R.; Inglese, J.; Yuan, J.; Roepe, P. D.; Su, X.; Thomas, C. J. High-Throughput Matrix Screening Identifies Synergistic and Antagonistic Antimalarial Drug Combinations. *Sci. Rep.* **2015**, *5*, 13891.
(58) Abraham, M. J.; Murtola, T.; Schulz, R.; Pall, S.; Smith, J. C.; Hess, B.; Lindahl, E. GROMACS: High Performance Molecular Simulations through Multi-Level Parallelism from Laptops to Supercomputers. *SoftwareX* **2015**, *1−2*, 19−25.
(59) Lindorff-Larsen, K.; Piana, S.; Palmo, K.; Maragakis, P.; Klepeis, J. L.; Dror, R. O.; Shaw, D. E. Improved Side-Chain Torsion Potentials for the Amber Ff99SB Protein Force Field. *Proteins: Struct., Funct., Genet.* **2010**, *78* (8), 1950−1958.
(60) Becker, J. P.; Wang, F.; Sonnet, P.; Dupradeau, F. Y. β-Hematin Crystal Formation: New Insights from Molecular Dynamics Simulations of Small Clusters in Condensed Phase. *Cryst. Growth Des.* **2016**, *16* (4), 2249−2259.
(61) Jorgensen, W. L.; Chandrasekhar, J.; Madura, J. D.; Impey, R. W.; Klein, M. L. Comparison of Simple Potential Functions for Simulating Liquid Water. *J. Chem. Phys.* **1983**, *79* (2), 926−935.
(62) Caleman, C.; van Maaren, P. J.; Hong, M.; Hub, J. S.; Costa, L. T.; van der Spoel, D. Force Field Benchmark of Organic Liquids: Density, Enthalpy of Vaporization, Heat Capacities, Surface Tension, Isothermal Com-Pressibility, Volumetric Expansion Coefficient, and Dielectric Constant. *J. Chem. Theory Comput.* **2012**, *8*, 61−74.
(63) Hess, B.; Bekker, H.; Berendsen, H. J. C.; Fraaije, J. G. E. M. LINCS: A Linear Constraint Solver for Molecular Simulations. *J. Comput. Chem.* **1997**, *18* (12), 1463−1472.
(64) Miyamoto, S.; Kollman, P. A. Settle: An Analytical Version of the SHAKE and RATTLE Algorithm for Rigid Water Models. *J. Comput. Chem.* **1992**, *13* (8), 952−962.
(65) Essmann, U.; Perera, L.; Berkowitz, M. L.; Darden, T.; Lee, H.; Pedersen, L. G. A Smooth Particle Mesh Ewald Method. *J. Chem. Phys.* **1995**, *103* (19), 8577−8593.
(66) Tanaka, H.; Gubbins, K. E. Structure and Thermodynamic Properties of Water–Methanol Mixtures: Role of the Water–Water Interaction. *J. Chem. Phys.* **1992**, *97*, 2626.
(67) Straaso, T.; Kapishnikov, S.; Kato, K.; Takata, M.; Als-Nielsen, J.; L, L. Experimental Crystal Structure Determination. *CCDC*; The Cambridge Crystallographic Data Centre, 2011; 841403, DOI: 10.5517/CCX7K1Q.
(68) Bussi, G.; Donadio, D.; Parrinello, M. Canonical Sampling through Velocity Rescaling. *J. Chem. Phys.* **2007**, *126* (1), 014101.
(69) Parrinello, M.; Rahman, A. Polymorphic Transitions in Single Crystals: A New Molecular Dynamics Method. *J. Appl. Phys.* **1981**, *52*, 7182.
(70) Nakouzi, E.; Stack, A. G.; Kerisit, S.; Legg, B. A.; Mundy, C. J.; Schenter, G. K.; Chun, J.; De Yoreo, J. J. Moving beyond the Solvent-Tip Approximation to Determine Site-Specific Variations of Interfacial Water Structure through 3D Force Microscopy. *J. Phys. Chem. C* **2021**, *125*, 1282.
(71) Araki, Y.; Tsukamoto, K.; Takagi, R.; Miyashita, T.; Oyabu, N.; Kobayashi, K.; Yamada, H. Direct Observation of the Influence of Additives on Calcite Hydration by Frequency Modulation Atomic Force Microscopy. *Cryst. Growth Des.* **2014**, *14* (12), 6254−6260.
(72) Fukuma, T.; Reischl, B.; Kobayashi, N.; Spijker, P.; Canova, F. F.; Miyazawa, K.; Foster, A. S. Mechanism of Atomic Force Microscopy Imaging of Three-Dimensional Hydration Structures at a Solid-Liquid Interface. *Phys. Rev. B: Condens. Matter Mater. Phys.* **2015**, *92*, 155412.
(73) Prihoda, A.; Will, J.; Duchstein, P.; Becit, B.; Lossin, F.; Schindler, T.; Berlinghof, M.; Steinrück, H.-G.; Bertram, F.; Zahn, D.; Unruh, T. Interface between Water−Solvent Mixtures and a Hydrophobic Surface. *Langmuir* **2020**, *36*, 12077.
(74) Reischl, B.; Raiteri, P.; Gale, J. D.; Rohl, A. L. Atomistic Simulation of Atomic Force Microscopy Imaging of Hydration Layers on Calcite, Dolomite, and Magnesite Surfaces. *J. Phys. Chem. C* **2019**, *123*, 14985−14992.
(75) Stumpe, M. C.; Blinov, N.; Wishart, D.; Kovalenko, A.; Pande, V. S. Calculation of Local Water Densities in Biological Systems: A Comparison of Molecular Dynamics Simulations and the 3D-RISM-KH Molecular Theory of Solvation. *J. Phys. Chem. B* **2011**, *115*, 319−328.
(76) Söngen, H.; Jaques, Y. M.; Zivanovic, L.; Seibert, S.; Bechstein, R.; Spijker, P.; Onishi, H.; Foster, A. S.; Kühnle, A. Hydration Layers at the Graphite-Water Interface: Attraction or Confinement. *Phys. Rev. B: Condens. Matter Mater. Phys.* **2019**, *100* (8), 205410−205411.
(77) Martiniano, H. F. M. C.; Galamba, N. Insights on Hydrogen-Bond Lifetimes in Liquid and Supercooled Water. *J. Phys. Chem. B* **2013**, *117* (50), 16188−16195.
(78) Debolt, S. E.; Kollman, P. A. Investigation of Structure, Dynamics, and Solvation in 1-Octanol and Its Water-Saturated Solution: Molecular Dynamics and Free-Energy Perturbation Studies. *J. Am. Chem. Soc.* **1995**, *117*, 5316.
(79) Chen, B.; Siepmann, J. I. Microscopic Structure and Solvation in Dry and Wet Octanol. *J. Phys. Chem. B* **2006**, *110* (8), 3555−3563.
(80) Rocchi, C.; Bizzarri, A. R.; Cannistraro, S. Water Dynamical Anomalies Evidenced by Molecular-Dynamics Simulations at the Solvent-Protein Interface. *Phys. Rev. E: Stat. Phys., Plasmas, Fluids, Relat. Interdiscip. Top.* **1998**, *57*, 3315.
(81) Ghosh Dastidar, S.; Mukhopadhyay, C. Structure, Dynamics, and Energetics of Water at the Surface of a Small Globular Protein: A Molecular Dynamics Simulation. *Phys. Rev. E: Stat. Phys., Plasmas, Fluids, Relat. Interdiscip. Top.* **2003**, *68*, 021921.

(82) Gallo, P.; Sciortino, F.; Tartaglia, P.; Chen, S.-H. Slow Dynamics of Water Molecules in Supercooled States. *Phys. Rev. Lett.* **1996**, *76*, 2730.
(83) Faraone, A.; Liu, L.; Mou, C. Y.; Yen, C. W.; Chen, S. H. Fragile-to-Strong Liquid Transition in Deeply Supercooled Confined Water. *J. Chem. Phys.* **2004**, *121* (22), 10843−10846.
(84) Petsev, D. N.; Wu, X.; Galkin, O.; Vekilov, P. G. Thermodynamic Functions of Concentrated Protein Solutions from Phase Equilibria. *J. Phys. Chem. B* **2003**, *107*, 3921−3926.
(85) Elhadj, S.; De Yoreo, J. J.; Hoyer, J. R.; Dove, P. M. Role of Molecular Charge and Hydrophilicity in Regulating the Kinetics of Crystal Growth. *Proc. Natl. Acad. Sci. U. S. A.* **2006**, *103* (51), 19237−19242.
(86) Vekilov, P. G. What Determines the Rate of Growth of Crystals from Solution? *Cryst. Growth Des.* **2007**, *7*, 2796−2810.

https://doi.org/10.1021/acs.jpcb.1c06589
J. Phys. Chem. B 2021, 125, 11264−11274